PAPER

Pedestal stability analysis on MAST in preparation for MAST-U

IOP Publishing | International Atomic Energy Agency Nuclear Fusion

Nucl. Fusion **61** (2021) 046041 (15pp) https://doi.org/10.1088/1741-4326/abe804

Pedestal stability analysis on MAST in preparation for MAST-U

M. Knolker[1,*], T. Osborne[1], E. Belli[1], S. Henderson[2], A. Kirk[2], L. Kogan[2], S. Saarelma[1] and P.B. Snyder[1]

[1] General Atomics, San Diego, CA 92186-5608, United States of America
[2] United Kingdom Energy Authority, Oxford, United Kingdom of Great Britain and Northern Ireland

E-mail: knolkerm@fusion.gat.com

Received 11 December 2020, revised 4 February 2021
Accepted for publication 19 February 2021
Published 18 March 2021

Abstract

In preparation for the upcoming MAST-U campaign, pedestal stability of spherical tokamaks is revisited by investigating standard H-mode discharges on MAST. As a step beyond previous studies, both ion and electron profiles are used for obtaining equilibria and a diverse set of pedestals is evaluated. Stability analysis with the ELITE and CGYRO codes shows that MAST pedestals are constrained by kinetic ballooning modes and medium toroidal mode number peeling-ballooning modes, with most unstable modes ranging from $n = 25$ to $n = 45$. In discharges with a steep q profile at the edge a larger number of poloidal harmonics is excited for each toroidal mode. A comparison with discharges on DIII-D with matched shape and similar non-dimensional parameters indicates that the increased shear at lower aspect ratio stabilizes low n peeling modes.

Keywords: spherical tokamak, pedestal, stability

(Some figures may appear in colour only in the online journal)

1. Introduction and state of the question

Spherical tokamaks are characterized by their small aspect ratio $A = \frac{R}{a} \sim 1.2$–2.0, with a the minor and R the major radius, resulting in access to higher values of elongation $\kappa = 1.5$–3, edge safety factor $q_{95} = 4$–20 and normalized beta $\beta_N = 3$–6 compared to standard tokamaks [1–3]. The attractiveness and promise of spherical tokamaks consists of achieving higher normalized plasma parameters than standard aspect ratio tokamaks with the same volume, thus reducing overall costs for potential future fusion power plants [4].

In general, a proven strategy for raising tokamak confinement is optimizing the H-mode pedestal [5], since it provides boundary conditions for both the core and divertor regions. The idea is readily explained: if the transport in the plasma core is limited by the onset of ion temperature gradient driven modes at a critical temperature gradient scale length, so-called profile stiffness, then given a relatively flat density profile a higher pedestal pressure will elevate the pressure profile in the core in proportion with the pedestal height, leading to a predicted scaling of fusion power with the square of pedestal pressure [6]. Hence, understanding and optimizing pedestal stability is vital in all tokamaks.

As with moderate aspect ratio tokamaks, the maximum pedestal pressure of spherical tokamaks in standard H-modes is limited by the onset of the peeling ballooning modes. The instability triggers edge localized modes, repetitive partial collapses of the edge transport barrier, leading to transient confinement degradation and expelling of particles and energy [7, 8]. Of particular interest is the type-I or giant ELM [7], since this type is ubiquitous in the standard H-mode scenario, the regime foreseen for ITER and future reactors. The pedestal conditions required for triggering giant ELMs are well explained by the peeling ballooning model, identifying current and pressure driven instabilities and their interplay as underlying cause [9].

In previous work, the type-I ELMy plasmas on MAST [10] were shown to reach the high n ($n = 35$–50) peeling-ballooning mode stability limit immediately before a giant ELM [11–13], whereas in work on NSTX [14], a comparable

* Author to whom any correspondence should be addressed.

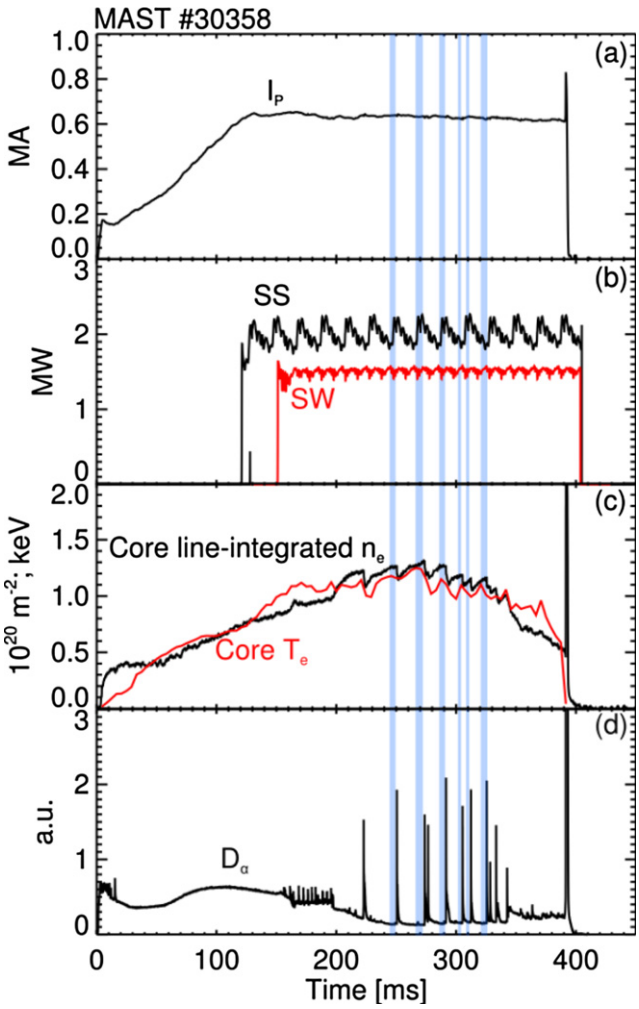

Figure 1. Discharge trajectory of a type I standard ELM H-mode on MAST (*a*) plasma current (*b*) NBI heating power by southwest (red) and south system (black) (*c*) line-integrated core density (black) and core electron temperature (red) (*d*) D–α recycling near the midplane. The 80%–99% time intervals prior to type I ELMs are shaded in blue.

spherical tokamak, low n peeling-ballooning modes were identified as the dominant instability [15–17]. Possible origins of this discrepancy could be physical and for instance originate from different fueling (MAST has a larger vacuum vessel, so the gap between plasma and outer wall is larger), or could be related in part to different measurement uncertainties including techniques for aligning electron and ion profiles.

Understanding the pedestal stability of spherical tokamaks is important for extrapolation towards future machines such as MAST-U [18] or power plants based on this concept since the response of the pedestal highly varies depending on the nature of its limitation: for instance, low n peeling-ballooning-modes are dominated by the peeling character (driven by the edge current gradient, resulting primarily from bootstrap current) and the pedestals limited by them tend to increase in height with density since the associated higher collisionality reduces the bootstrap current, whereas ballooning dominated pedestals react negatively to bootstrap current reduction, as this increases magnetic shear.

Hence, the scope of this paper is undertaking pedestal stability analysis on MAST standard H-modes with type I ELMs on a diverse set of pedestals (sections 2 and 3). Moreover, a broadening of the understanding is attempted by comparing results to matched discharges of the DIII-D tokamak [19] (section 4), and ultimately extrapolating to MAST-U (sections 5 and 6).

2. Experimental setup and diagnostics

To ensure generality in the edge stability analysis on MAST, wide ranges of relevant parameters, such as pedestal temperature and collisionality, need to be covered. Hence, a discharge selection was made from several MAST campaigns spanning half a decade of research. The on-axis toroidal magnetic field in the dataset ranges from $B_T = 0.4$–0.5 T, plasma current is $I_P = 0.5$–0.9 MA and injected neutral beam powers are $P_{NBI} = 1.5$–3.5 MW. The plasma shapes are in single and double null configuration, spanning average triangularities of $\delta = 0.35$–0.5 and elongations $\kappa = 1.7$–2.0.

Electron profiles on MAST are measured with a Thomson scattering diagnostic consisting of two systems [20, 21], providing a spatial resolution down to 5 mm. Characteristics of ions are evaluated with a charge exchange recombination system (CER) [15]. Furthermore, neutron rates are monitored with a system of several detectors [22] and used to constrain the anomalous diffusion rates necessary to determine the fast ion profile, as explained in the later segments of this section.

A typical discharge trajectory is shown in figure 1. Following a ramp in the plasma current (*a*), core density and temperature (*c*) are rising, supported by the injection of neutral beam power (*b*) from both the south and southwest system. Heating power is kept constant in these discharges, so that the pedestal conditions outside of the ELM cycle remain relatively stationary. The LH-transition occurs at 0.15 s and is initiated with type III dithering ELMs, visible in the D–α recycling trace (*d*). Once a sufficiently high density is reached, the plasma can access the type I ELM regime. The green shaded areas mark the 80%–99% inter-ELM intervals, which are used for obtaining profiles for the pedestal stability analysis.

A representative set of profiles for this discharge is shown in figure 2. In general, the raw measurement data is collected over a time window of 80 ms to 200 ms (here from 0.25 s to 0.33 s) and then conditionally averaged over the 80%–99% inter-ELM interval. Typically, the core plasma profiles are fit using polynomials and the edge profiles with a spline or the well-established hyperbolic tangent fit [23]. As can be seen, the electron density n_e is monotonically decreasing in the core but has a small rise in the core-edge blending region next to the step gradient edge (*a*). Previous analysis has shown that carbon is the dominant impurity on MAST, and helium is present as well due to glow cleaning between discharges [24, 25]. Since there is neither helium nor carbon impurity density measurement, the helium contribution is neglected and carbon density n_C (*e*) has to be inferred assuming a radially constant effective charge, typically in the range of $Z_{eff} = 1.5$–2. The impact of this choice for stability is evaluated in the appendix A of this paper. Since neutral beam injection is the dominant heating

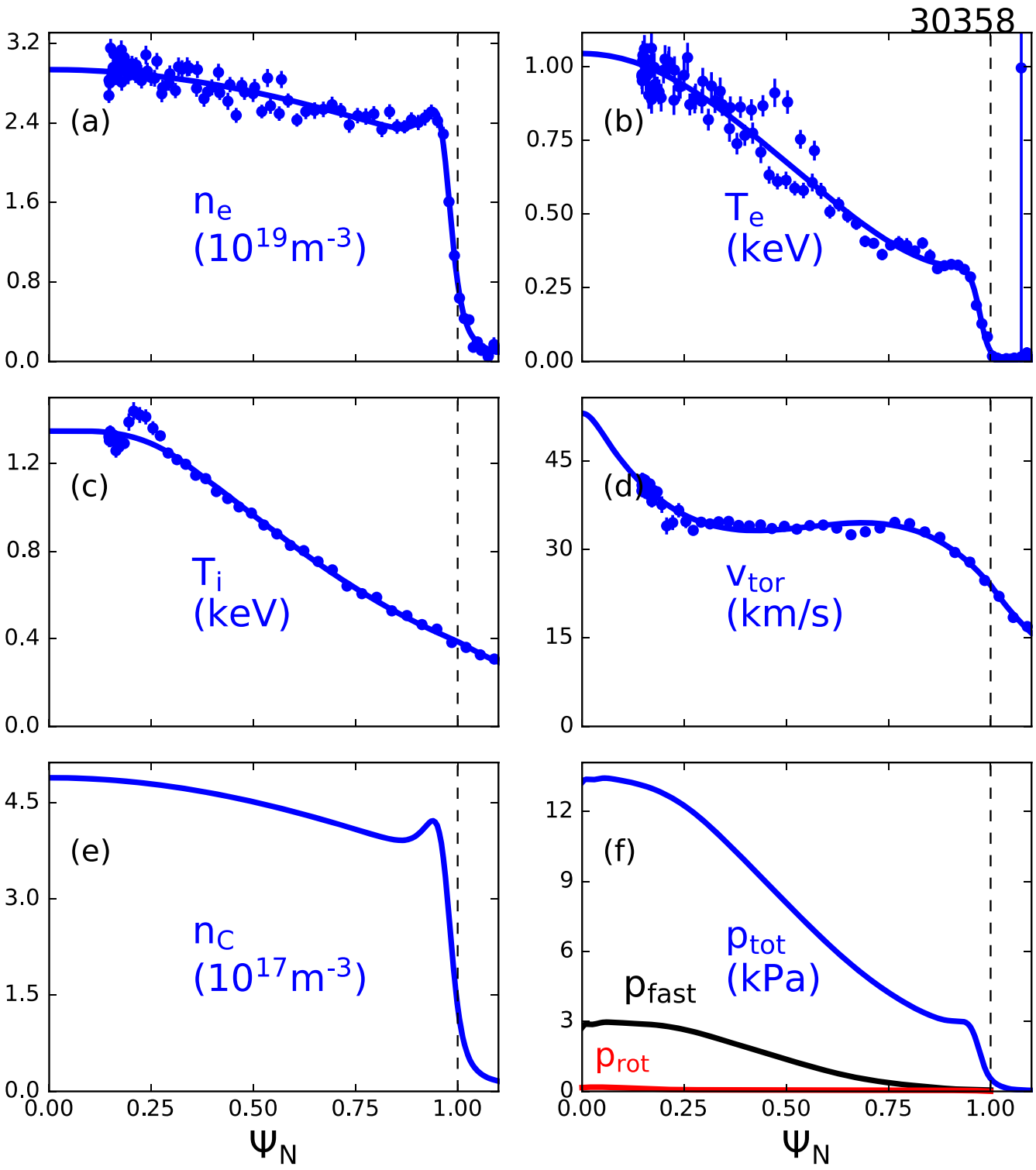

Figure 2. Obtained profiles from conditionally averaging over the 80%–99% inter-ELM phase; (*a*) electron density and (*b*) temperature, (*c*) ion temperature and (*d*) toroidal rotation as measured by CER, (*e*) calculated carbon impurity density (*f*) fast ion pressure (black), rotational pressure (red) and total pressure (blue).

source in these discharges, the ion temperature T_i (*c*), strongly exceeds the electron temperature T_e in the edge region (*b*). The origin of the temperature scatter around $\psi_N \sim 0.4$ is due to alignment issues between HFS and LFS. This paper follows the standard approach on MAST of including data from both sides into the temperature profile. For all discharges used in the subsequent analysis good agreement in the pedestal region was required, whereas alignment discrepancies in the core region are in general of rather minor influence for pedestal stability and hence acceptable for this work. A toroidal rotation measurement of the carbon ions v_{tor} (*d*) is used to measure the plasma rotation. For this discharge, the plasma center rotates

with 45 km s^{-1} toroidally. Fast ion profiles are generated using TRANSP [26, 27]. Significant anomalous diffusion with a coefficient on the order of 2.0–4.0 m^2 s^{-1} is required to match the neutron rates with experimental values. The TRANSP calculated neutron rate is mainly based on beam-target collisions with a negligible fraction of thermal fusion neutrons and beam–beam collisions. The fast ion and total pressure profiles are shown in (f). The latter resembles the typical standard H-mode tokamak profile features, namely a pedestal upon which the plasma core resides. Depending on the discharge, net rotational energy contributions amount to 0.5–2.5 kPa (red) and are hence not significant for MAST.

There are two important alignment choices that have to be made for the profile fitting:

- Symmetrization: due to the strong variation of the major radius between high and low field sides in spherical tokamaks the spacing between flux surfaces also varies strongly. This can make the high and low field side measurements difficult to align. Hence an algorithm-based optimization is undertaken, aiming to minimize residuals in the overlaying fits of high and low field side by orienting and shifting measurement points on the respective flux surfaces. Since the CER system is strongly focused on the low field side [28], a symmetrization for ion measurements is not necessary, by exclusively using LFS data.
- Finding the appropriate separatrix temperature $T_{e,sep}$: based on heating power, $T_{e,sep}$ is chosen between 35–50 eV (resulting in an ion separatrix temperature ranging between 120–180 eV). A bad choice of separatrix temperature can lead to a bad alignment between magnetics and Thomson profiles and result in a non-convergence of the Grad–Shafranov equation computed by EFIT [29], in which case the fitting process is iterated with a different temperature choice.

In a final step towards the equilibrium, the thermal and fast ion pressure profiles are mapped on magnetic surfaces to set the total pressure profile in the kinetic EFITs. A kinetic EFIT is an axisymmetric solution to the toroidal equilibrium, as described by the Grad–Shafranov equation, constrained by magnetic probe and flux loop data, by the plasma pressure profile, and by setting the current density in the pedestal region to the sum of the bootstrap current computed using the Sauter model [29, 30] plus smaller contributions from ohmic and neutral beam driven currents. For this purpose, EFIT++ is used. EFIT++ is a substantial rewrite of the original EFIT code [29], able to handle arbitrary tokamak configurations and compute induced currents among others. For higher resolution and better agreement with the experimental measurement in the pedestal region, the results of EFIT++ are processed again with a modified EFIT version. The latter is enhanced with a solver allowing for an arbitrary boundary shape. The boundary shape is set to the separatrix determined from the EFIT++ fit. The current density is determined as the sum of the bootstrap current from the kinetic profiles and an 'ohmic' current which in the core is given by the initial equilibrium while being assumed to be fully resistively relaxed in the pedestal region.

Figure 3 visualizes the range of selected parameters covered by experimental equilibria reconstructed as described above. The pressure gradient drive for the peeling-ballooning mode is generally expressed in terms of the normalized pressure gradient α [31]

$$\alpha = \frac{\mu_0}{2\pi^2}\frac{\partial V}{\partial \psi}\left(\frac{V}{2\pi^2 R}\right)^{\frac{1}{2}}\frac{\partial p}{\partial \psi}. \tag{1}$$

Here, μ_0 is the vacuum permeability, V is the volume enclosed by a flux surface with the poloidal flux ψ, R is the plasma major radius and p the pressure. In general, α is growing with the safety factor (and smaller plasma currents) (figure 3(a)), which is expected based on simplified derivations for circular plasmas if the pressure gradient is kept fixed, resulting in [32].

$$\alpha = 2\mu_0 \frac{Rq^2}{B^2}\frac{\mathrm{d}p}{\mathrm{d}r}. \tag{2}$$

The pedestal pressure range covered ranges from 1.5–2.2 kPa (figure 3(b)) with pedestal temperatures up to about 300 eV.

Transitioning to peeling modes, the edge current consists of contributions from externally driven currents j_{drive} (by ohmic induction, neutral bream heating), Pfirsch Schlueter currents j_{PS} (parallel to magnetic field on LFS, antiparallel on HFS) and the bootstrap current j_{bs}.

$$j = j_{drive} + j_{PS} + j_{bs}. \tag{3}$$

While the current density in the core is mainly driven by ohmic contributions, by far the largest contribution to the edge current density comes in form of the bootstrap current density where the leading order term in the Sauter expression is also proportional to edge density and temperature gradients [30]

$$j_{bs} = I_P(\psi)\cdot p_e \cdot \left(\frac{A}{p_e}\frac{\partial p}{\partial \psi} + \frac{B}{T_e}\frac{\partial T_e}{\partial \psi} + \frac{C}{T_i}\frac{\partial T_i}{\partial \psi}\right) \tag{4}$$

with the pressure gradient term typically strongly dominating in the expression. In general, the coefficients A, B and C increase with trapped particle fraction $f_t \sim \frac{r}{R}$ but decay with increasing collisionality ν_e^*. The latter is typically compared at the pedestal top and calculated via [30]

$$\nu_e^* = 6.921\times 10^{-18}\cdot q_{95}\cdot R_{max}\cdot n_{e,ped} \frac{Z_{eff}\cdot\left(31.3 - \ln\frac{{n_{e,ped}}^{0.5}}{T_{e,ped}}\right)}{{T_{e,ped}}^2\cdot\left(\frac{a}{R_{Surf}}\right)^{1.5}}, \tag{5}$$

where R_{Surf} is the major radius of the center of the outermost closed flux surface, and all quantities with subscript ped refer to the respective value at the pedestal top. The pedestal electron collisionalities in the MAST discharges studied ν_e^* was between 0.3–3.4. Collisionality is a measure for how often electrons at the plasma edge collide relative to the banana orbit bounce frequency. Note that in the investigated MAST dataset, a large span of ν is covered for high pedestal pressure, in order to evaluate the influence of collisionality and improve extrapolation to MAST-U. The current drive for the peeling ballooning

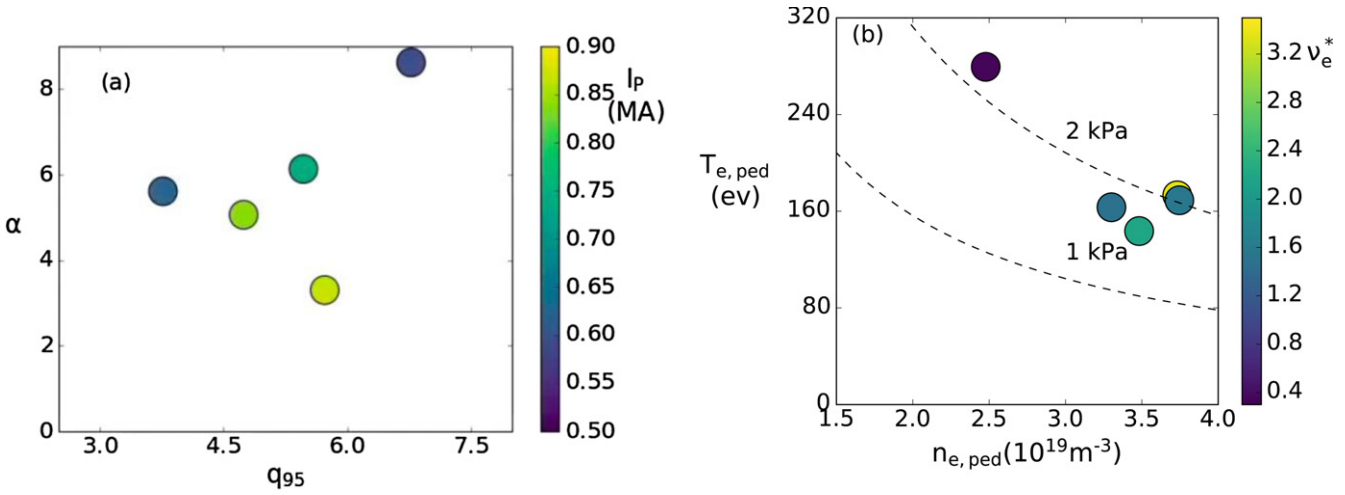

Figure 3. Overview of kinetic equilibria in different parameter spaces (*a*) dependence of maximum of normalized pedestal pressure gradient on safety factor and plasma current (*b*) pedestal temperature and density with their respective collisionality.

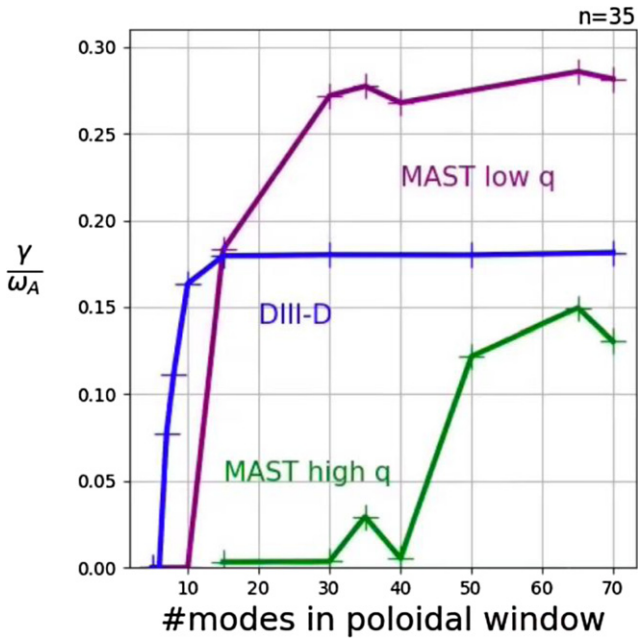

Figure 4. Growth rates in dependence of poloidal mode number window size for an $n = 35$ peeling-ballooning mode on a matched DIII-D discharges with $q_{95} = 2.8$ (blue) and two MAST equilibria with $q_{95} = 3.8$ (purple) and $q_{95} = 6.8$ (green).

mode is expressed in terms of the normalized pedestal current density $\bar{j}$, defined as ratio of separatrix current density j_{sep} and maximum current density j_{max}in the edge to the average current density j_{av}

$$\bar{j} = \frac{j_{sep} + j_{max}}{2 j_{av}}. \tag{6}$$

The quantity is hence a measure both for peakedness of the edge current profile and overall edge current fraction.

To understand the complex interplay between current and pressure driven modes at the edge, it is important to realize that edge currents are reducing the magnetic shear *s*, defined as

$$s = \frac{r}{q}\frac{\mathrm{d}q}{\mathrm{d}r} \tag{7}$$

which is stabilizing for ballooning modes [9].

To summarize, this section has described the process for obtaining profiles and equilibria on MAST and building a database, demonstrating its generality and repeatability with the caveats of several necessary choices (separatrix temperature, LFS/HFS alignment). Unique features of the low aspect ratio machine that could influence pedestal stability are the high safety factor and resulting large normalized pressure gradient. The discharges used for the comparison with DIII-D and their experimental setup are described in section 4.

3. Pedestal stability analysis

3.1. Physics of edge modes in low aspect ratio tokamaks

Prior to conducting peeling ballooning stability analysis on the generated equilibria, the primary physics effects of low aspect ratio and high safety factor were considered to optimize the stability calculations. This mainly concerns the number of poloidal modes excited for each toroidal mode number. Due to the high safety factor and magnetic shear, resonant surfaces are closer to each other in the edge region then is typical at higher aspect ratio, facilitating coupling of a large number of poloidal modes. In addition, low aspect ratio leads to stronger coupling of poloidal modes (at infinite aspect ratio, poloidal modes are uncoupled). Due to the combination of these effects, MHD stability codes such as ELITE [9], which use a poloidal mode decomposition, require substantially larger numbers of poloidal modes to reach convergence than in typical cases at moderate aspect ratio. To illustrate the contrast between MAST and DIII-D, growth rates as a function of the number of poloidal modes included are shown for an $n = 35$ mode on DIII-D and MAST for cases with matched cross-sectional shapes (figure 4). While a more detailed shape comparison and discharge parameter overview are discussed later in this paper, the interest reader is referred to table 1 and figure 10. One

Table 1. Overview of selected MAST and DIII-D discharges based on kinetic equilibria.

	MAST (R/a) = 1.3			DIII-D (R/a) = 2.9		
Shot	29795	30422	24763	30358	122804	122811
B_T (T)	0.4	0.4	0.5	0.4	0.5	0.8
I_P (MA)	0.6	0.7	0.8	0.6	0.6	0.8
P_{NBI} (MW)	3.5	3.5	3.5	3.5	1.5	1.2
κ	2.0	1.7	1.7	1.7	1.7	1.7
δ (δ_{min})	0.5 (0.4)	0.5 (0.5)	0.5 (0.5)	0.4 (0.2)	0.5 (0.5)	0.5 (0.4)
q_{95}	6.8	5.3	4.9	3.8	2.4	2.8
β_N	4.2	3	3.3	3.0	2.2	1.9
p_{ped} (kPa)	1.6	1.8	2.2	2.8	2.8	2.5
$T_{e,ped}$ (keV)	0.16	0.17	0.17	0.28	0.24	0.23
ν_e^*	3.4	2.2	1.6	0.4	4.0	4.1
Z_{eff}	1.5	1.6	1.6	1.5	3.8	3.1
α	8.8	6.1	4.7	5.6	4.0	4.2
j_N	0.56	0.55	0.46	0.70	0.52	0.44
s	8.9	10.2	8.8	5.5	4.0	3.5
$\beta_{pol,ped}$	0.19	0.14	0.13	0.23	0.35	0.18
f_{bs} (%)	22	16	12	16	10	13

can see that the growth rate reaches saturation for 15 poloidal modes on DIII-D (blue), whereas on MAST up to 50 modes can be necessary for convergence.

In addition, to resolve the fine structure of high n ballooning modes numerically, the ELITE radial mesh has to be refined to 2049 points instead of the 513 typically used for DIII-D runs, while the EFIT equilibrium rectangular grid resolution must be increased to 513×513 instead of 129×129. This comes at the cost of higher memory use and computational time required by ELITE and EFIT: up to 30 times more computational time is required compared to a standard DIII-D calculation at the same toroidal mode number.

For the illumination of the pedestal stability limitation, a set of equilibria is generated for each discharge using the VARYPED code [33] in fixed boundary mode (figure 5). The original equilibrium is indicated by the blue line and the envelope function symbolizes the range of equilibria with higher and lower pedestal pressure (a) and current densities (b). While in the original kinetic equilibrium the current density in the pedestal is set by the measured temperature and density profiles through the computed bootstrap and ohmic currents in addition to the magnetics measurements, the pedestal pressure and current density are varied independently in the VARYPED code keeping the plasma shape fixed to map the peeling-ballooning mode stability boundary as a function of normalized current density $\overline{j}$ and α.

While the pedestal quantities are varied the overall beta (a) and total toroidal current, and respectively safety factor at the separatrix (b) are held fixed. In a typical setup both normalized edge pressure gradient and current are varied from about a third to twice their experimental value.

Based on the pressure-current scan in figure 5, an example of a resulting MAST peeling ballooning stability diagram is shown in figure 6(a). The x-axis represents the normalized pressure gradient α, the y-axis normalized current density $\overline{j}$. For each equilibrium in the VARYPED scan ELITE is run for

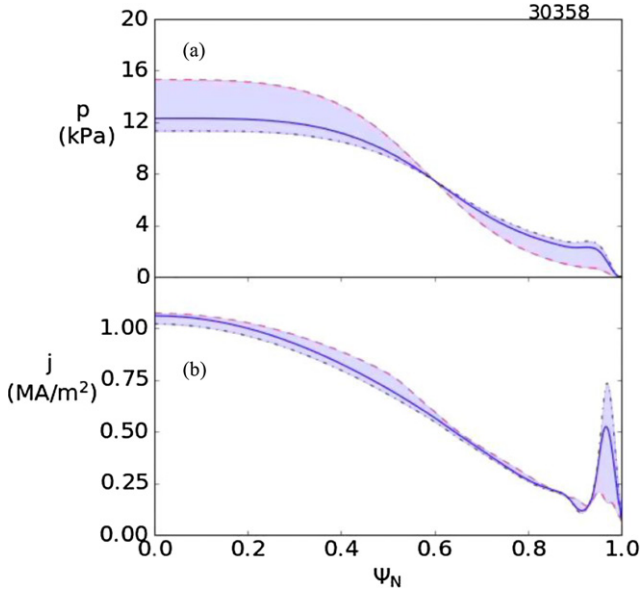

Figure 5. Variation of plasma pedestal pressure and edge current with VARYPED on MAST discharge 30358. Original equilibrium in blue with envelope function showing the extent of the scan.

toroidal mode numbers ranging from 5 (the minimum achievable in the ELITE implementation used) to 50, and the stability boundary is defined by the points where the maximum growth rate as a function of n exceeds 10% of the Alfven frequency. As is typical, the stability boundary blends low n current driven peeling modes with high n pressure gradient driven ballooning modes. Within the scanned region, the peeling boundary is far from the experimental point. Since the pedestal electron collisionality ν_e^* is rather low in this case and lower collisionality permits a higher bootstrap current, one might expect a stronger peeling character. For instance, equilibria on DIII-D with comparable collisionality are located on the peeling side, or at the intersection of peeling and ballooning side ('nose' of the

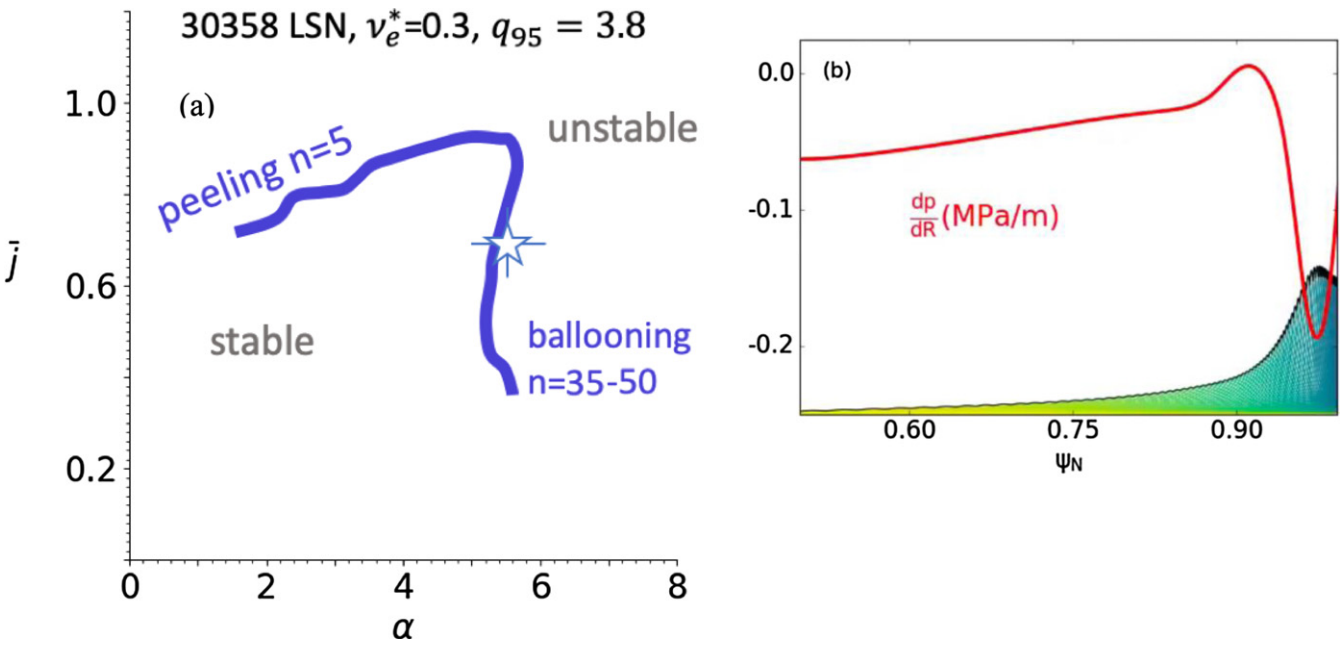

Figure 6. (*a*) Peeling ballooning map for a low collisionality, LSN MAST discharge (*b*) eigenfunction of unstable $n = 35$ mode with overlay of pressure gradient.

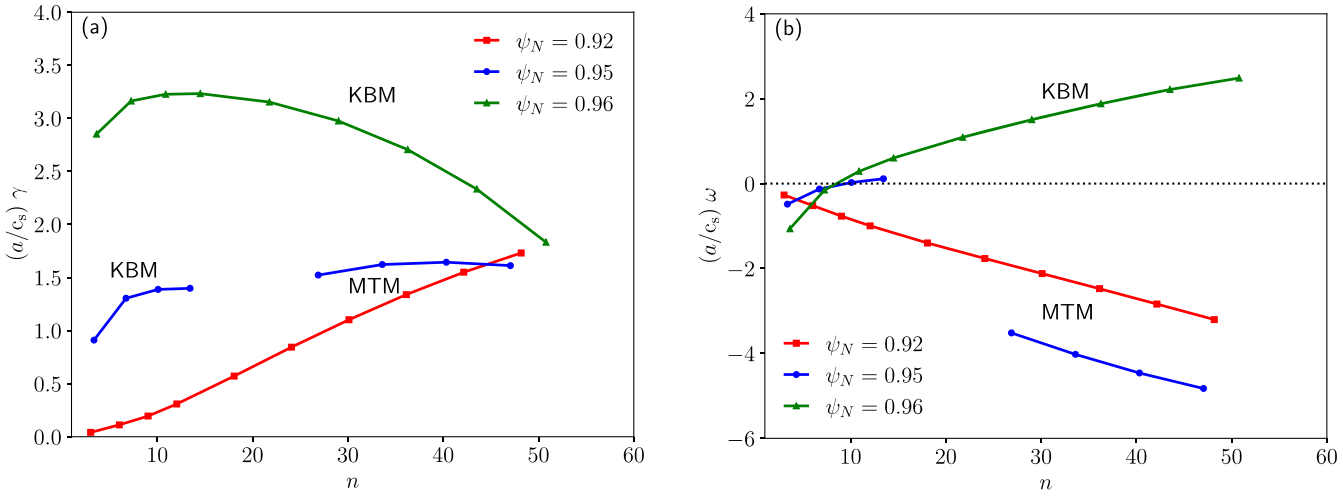

Figure 7. CGRYO analysis of discharge 29795: growth rate (*a*) and real frequency (*b*) of the most unstable drift mode vs toroidal mode number n for various locations in the pedestal region.

peeling ballooning diagram) [34]. Note that $Z_{\text{eff}} = 1.5$ was assumed on the lower end of its expected range so that the experimental value for the collisionality ν_e^* may in fact be higher and so $\bar{j}$ lower and even further from the peeling limit.

The most unstable mode at the experimental point is found in the $n = 35$–40 range and the $n = 35$ radial eigenfunction combining many poloidal modes is shown in figure 6(*b*). It peaks around $\psi_N = 0.97$ near the peak of the pressure gradient as is typical. The results presented above are representative for the array of analyzed equilibria and also agree with results from previous stability analysis on MAST that was based on electron profile measurements only [11, 13].

3.2. Kinetic effects in low aspect ratio tokamaks

At the low magnetic field values in MAST and the expected high toroidal mode numbers for the peeling-ballooning modes the poloidal mode width can be comparable to the ion gyro radius. Therefore kinetic effects may be important and the predictions of ELITE as a linear MHD calculation may not be valid. For the equilibrium with the highest $q_{95} = 6.8$ in our dataset, the calculated poloidal mode width for an $n = 35$ toroidal mode and the ion gyro radius are both approximately 0.02 m. To check the validity of ELITE under these conditions we compare its results to those of the local electromagnetic gyrokinetic CGYRO code [35, 36], where the growth rate of

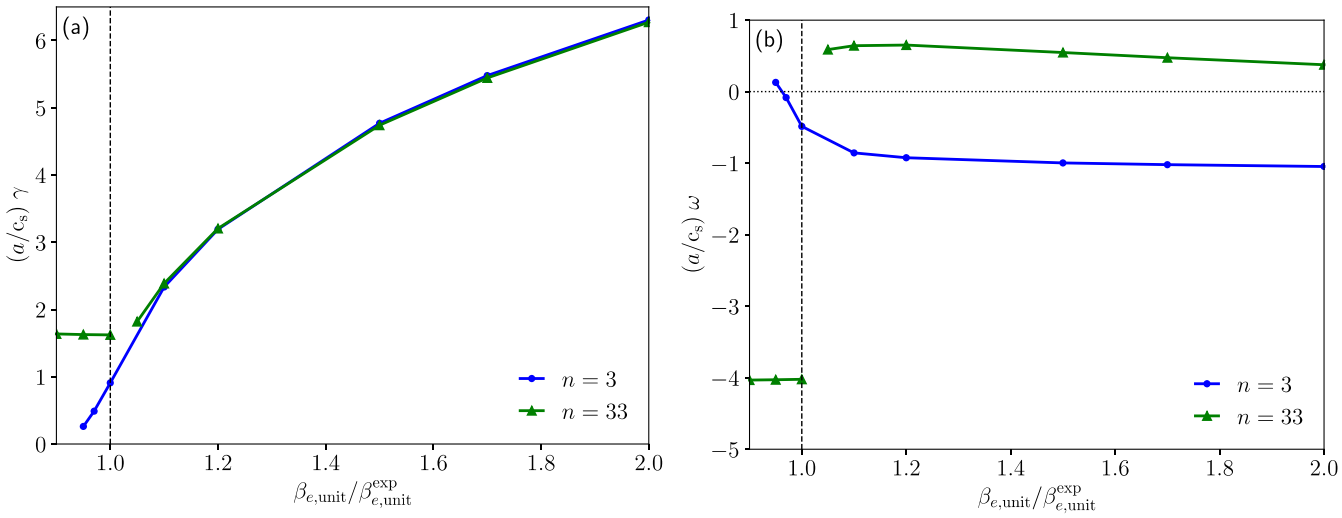

Figure 8. CGRYO analysis of discharge 29795: growth rate (*a*) and real frequency (*b*) of the most unstable drift mode vs the electron beta (relative to the experimental value) for low and high toroidal mode number at $\psi_N = 0.95$.

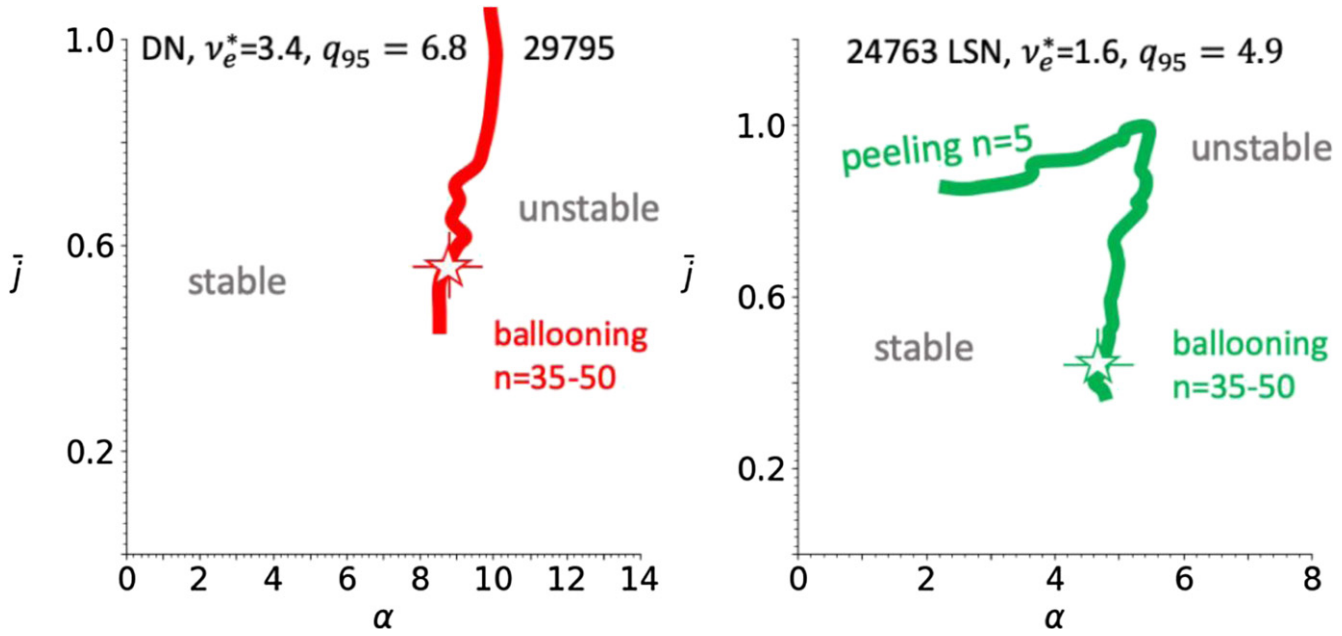

Figure 9. Pedestal stability analysis on selected MAST equilibria (*a*) double null shape with high collisionality and safety factor (*b*) medium collisionality, and lower safety factor equilibrium closer to the peeling boundary.

the most unstable mode is calculated as a function of mode number n and evaluated for various locations in the pedestal (figure 7).

With regards to sign convention, modes rotating in the ion direction are positive and modes rotating in the electron direction negative. For $\psi_N = 0.92$ just before the pedestal, the most unstable drift mode rotates in the electron direction and the eigenmode has tearing parity characteristic of a micro-tearing mode (MTM). In the pedestal region at $\psi_N = 0.95$ this mode dominates for high n modes above 30, while a kinetic ballooning mode (KBM) dominates at low n and for the entire n range at $\psi_N = 0.96$. Figure 8 shows that the strong beta dependence of the KBM. The KBM is close to threshold at the experimental level, such that, for the high-n MTM, a marginal increase in beta strongly drives the KBM and the MTM quickly becomes sub-dominant. Thus, in the pedestal the ballooning mode can persist with large growth rate to high n without significant FLR stabilization. Overall, the analysis with CGYRO confirms the dominance of a ballooning mode over most of the pedestal and shows that medium to high n KBMs are strongly unstable, and would be expected to drive large transport and constrain the pedestal pressure gradient, and therefore the pedestal height at a given width. This finding is in agreement with previous analysis [12, 37], where the formation of the pedestal throughout the ELM cycle on MAST was described as a competition process between a KBM in the step gradient region and an MTM localized near the pedestal top. Since the kinetic corrections do not alter the results significantly, and we wish to study

current-driven as well as pressure-driven modes, the following analysis on the full range of discharges is conducted using ELITE.

3.3. Overview of dataset

Selected peeling ballooning stability maps as calculated by ELITE for various equilibria introduced in figure 3, are shown in figure 9. All equilibria are medium to high n ballooning limited with critical mode numbers in the range of 35–50. Note that intermediate modes with $n = 10$–30 are gradually limiting the available space on the ballooning side in these discharges, but smaller in growth rates than the dominant high n mode. The biggest difference between the equilibria is the proximity to the peeling boundary. The high safety factor, high collisionality DND discharge 29795 ($q_{95} = 6.8$, $\nu_e^* = 3.4$, figure 9(a)) is purely ballooning limited within the scanned segment, so that not even a doubling of the edge current would trigger the peeling limit. On the other end, for a low collisionality discharge as 30358 ($q_{95} = 3.8$, $\nu_e^* = 0.3$), the bootstrap current is considerably higher and the equilibrium—while still limited by higher n peeling-ballooning modes and hence on the ballooning side—is approaching the peeling boundary (figure 6). Due to the medium to high range of collisionality, most cases are similar in appearance to discharge 24763 (shown in figure 9 (b)), where approximately a doubling of the normalized edge current is required to get to the peeling limit. When comparing the q-profiles near the peeling limited region for these discharges, the peeling limit coincides with q-profile becoming flat or reversed near the edge due to the large size of the bootstrap current. This indicates that a large reduction of shear in the edge is associated with approaching the peeling boundary.

This section has shown that MAST pedestals are limited by medium to high n peeling ballooning modes and their kinetic equivalent.

4. Comparison to DIII-D

In order to evaluate the influence of aspect ratio on pedestal stability, DIII-D discharges with matched MAST shapes from a multi machine pedestal scaling study [38] were selected with the goal of matching pedestal parameters (see figure 10). A MAST discharge (30358) with different shape, but very low collisionality is added to provide additional insights. An overview of the selected discharges is shown in table 1. The pedestal poloidal beta in the table is defined as $\beta_{\mathrm{pol,ped}} = \frac{p_{\mathrm{ped}}}{\frac{B_{\mathrm{pol}}{}^2}{2\mu_0}}$.

Within the matched shape MAST discharges (29795, 30422, 24763), a span from high to low safety factor and normalized pressure gradient is covered. The discharge with the highest q_{95} and lowest plasma current has the lowest pedestal pressure but highest normalized β_N. Since the bootstrap current fraction scales with the poloidal beta $f_{\mathrm{bs}} \sim \sqrt{\frac{a}{R}}\beta_{\mathrm{pol}}$ [30] and the poloidal beta increases with β_N and κ [39]

$$\beta \cdot \beta_{\mathrm{pol}} = 25\frac{1+\kappa^2}{2}\left(\frac{\beta_N}{100}\right)^2 \tag{8}$$

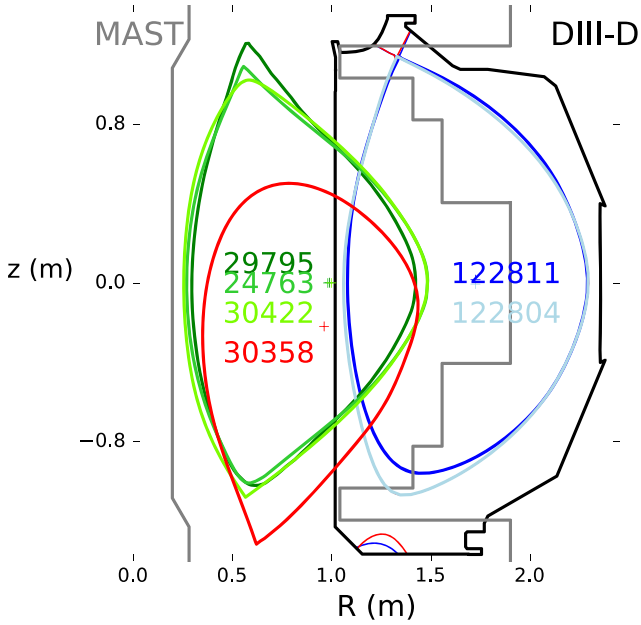

Figure 10. Shape comparison of matched MAST (green) and DIII-D (blue) discharges. Added MAST discharge for study of low collisionality effects (red).

discharge 29795 has the highest bootstrap current fraction of 22% within the type I ELM dataset. Despite of its high β_{pol} and low collisionality, discharge 30358 comes with a smaller bootstrap current fraction than 29795 due the low safety factor.

For the DIII-D matched cases, both have an elongation of 1.7 and an average triangularity of 0.5, but in the case of 122811 this is achieved by an upper triangularity of 0.6 and a lower triangularity of 0.4, whereas on 122804 this is achieved in a symmetric way. It has been shown elsewhere that the lower value of both triangularities is a better indicator for pedestal behavior than the mean [40]. The resulting peeling ballooning stability diagram for the DIII-D discharges 122811 and 122804 are shown in figure 11. The most unstable mode in both cases is $n = 40$ with a clear ballooning limited plasma.

Compared to MAST discharges, the noticeable differences for matched plasma shapes emerge from the lower safety factors and consequently reduced shear on DIII-D. Due to the higher aspect ratio at similar current and magnetic field, the edge safety factor is lower than on MAST, with leads to generally lower shear assuming that the central safety factor is about 1.0. The latter is deduced from the absence of sawtooth and fishbone activity. In addition, pedestal temperatures are higher on DIII-D, despite the reduced heating power (see table 1). The higher pedestal temperature explains why DIII-D discharges have similar collisionality despite the higher effective charge. For matched poloidal betas, the bootstrap current fraction on DIII-D is smaller than on MAST.

In direct comparison of pedestal stability results (figures 11 vs 6 and 9), one can see that DIII-D discharges are closer to the peeling limit. Note that the normalized current on the y-axis in the ELITE plots can be seen as a proxy for the bootstrap fraction in the pedestal and is similar or higher on MAST for similar pedestal conditions. If the peeling limit were the same one would expect MAST to be stronger peeling limited, so

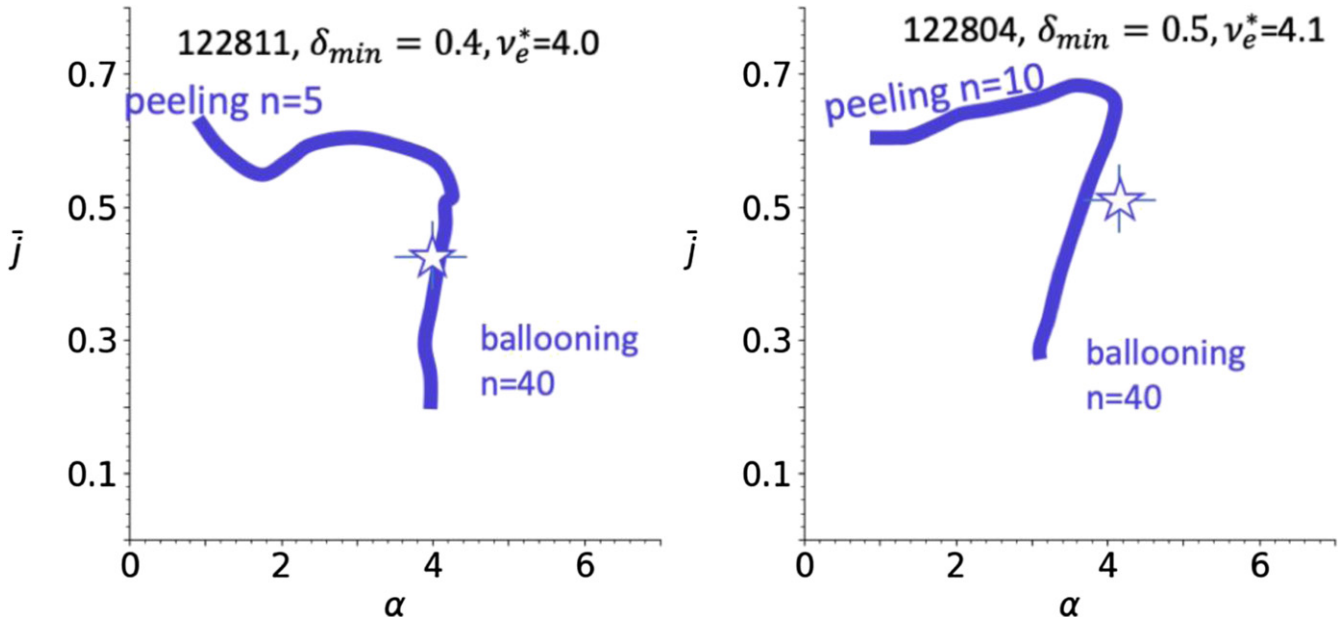

Figure 11. Pedestal Stability analysis on matched DIII-D discharges with (*a*) asymmetric and (*b*) symmetric triangularity.

consequently the peeling stability must be significantly better. Only the MAST case with very low collisionality (30358) gets similar proximity to the peeling limit as the DIII-D cases. This might be surprising given the facts that (*a*) the bootstrap current fractions are higher on the MAST discharges and more current drive destabilizes peeling modes (see ELITE plots) and (*b*) the enhanced stabilizing magnetic field line curvature allowing confined particles to spend more time on the high field side relative to large aspect ratio machines is expected to stabilize ballooning modes.

Stability criteria for peeling modes have been defined several times [41, 42], and to understand the impact of aspect ratio, edge current and shear, it is intuitive to follow [9, 43] and to consider the stability criterion for a simplified cylindrical torus [43]

$$\sqrt{1 - D_{\mathrm{M}}} > 1 + \frac{1}{\pi q'} \oint \frac{j_{\parallel} B}{R^2 B_{\mathrm{p}}^3} \mathrm{d}l, \tag{9}$$

where $q' = \frac{\mathrm{d}q}{\mathrm{d}\psi}$, B_{p} the poloidal field strength and D_{M} is the Mercier index [44]. The integration is executed poloidally along a flux surface. In the limit of $\varepsilon \ll 1$, D_{M} can be approximated as $D_{\mathrm{M}} = \frac{\alpha\varepsilon}{s^2}(\frac{1}{q^2} - 1)$. While neither DIII-D nor MAST are fulfilling $\varepsilon \ll 1$, this approximation ignoring finite aspect ratio effects suffices as definition of a general threshold for our considerations, since the interesting physics is happening on the right-hand side of the equation. From the simplified Mercier index, one can see, that larger normalized pressure gradient and inverse aspect ratio will increase the left-hand side of equation (9), while higher shear will reduce the right-hand side and hence permit higher tolerable parallel currents in the integral and stabilize peeling modes. Hence the proximity to this simplified peeling limit is closer on DIII-D discharges as shown in figure 12.

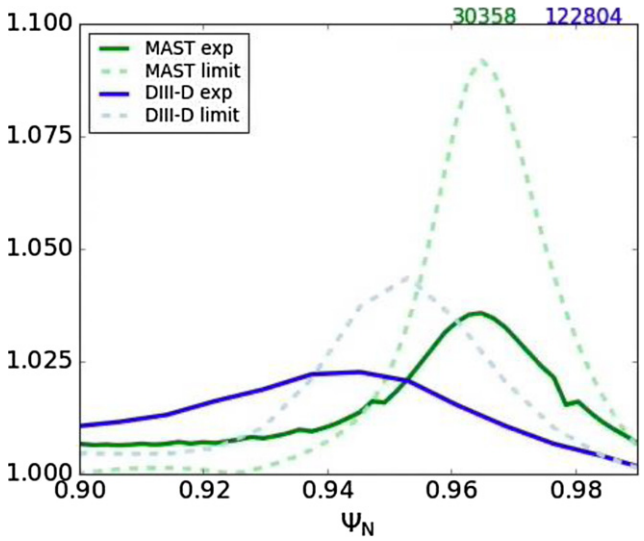

Figure 12. Simplified peeling stability criterion based on equation (9) for selected discharges listed in table 1. The left-hand side of equation (9) is plotted in form of dashed curves for each discharge, the solid curves express the right-hand side.

Since the shaping is approximately matched in this comparison, one can make further simplifications in equation (9), assuming low shaping and $\beta \ll 1$, arriving at [43]

$$\alpha \left[\frac{r}{R} \left(1 - \frac{1}{q^2} \right) + s\Delta' - f_{\mathrm{t}} \frac{Rs}{2r} \right] > Rqs \left(\frac{j_{\mathrm{drive}}}{B} \right)_{\mathrm{edge}}. \tag{10}$$

The first two terms are stabilizing, with the second one being the Pfirsch–Schlueter contribution, scaling with the Grad Shafranov shift Δ'. The third term is the destabilizing contribution of the bootstrap current, overall rising with aspect

ratio, since $f_t \sim \sqrt{\varepsilon}$. Further simplifying with equation (2), one arrives at

$$-\frac{dp}{dr}\frac{2q}{B^2}\left[\frac{\varepsilon}{s}\left(1-\frac{1}{q^2}\right)+\Delta'-f_t\frac{1}{2\varepsilon}\right] > \left(\frac{j_{drive}}{B}\right)_{edge}. \quad (11)$$

Here, one can see clearly that since destabilizing, bootstrap current related term $f_t\frac{1}{2\varepsilon} \sim \frac{1}{\sqrt{\varepsilon}}$ is shrinking with inverse aspect ratio, while the stabilizing terms are similar or higher on MAST.

β_N is higher on the MAST discharges, raising the Shafranov shift and stabilizing the pedestal, as confirmed in [45], while shear and inverse aspect ratio approximately balance each other in the first term (compare to table 1).

To better understand the result, peeling stability can be interpreted as a competition between stretching of the field lines (stabilizing) and attraction of the helical current filament to itself (destabilizing). As the filament is twisted to bring it closer to itself, the more toroidal the current filaments is, the more stretching is required. For the same plasma current and magnetic field ratio field lines are more toroidal at low aspect ratio, hence there is enhanced peeling stability.

Note that even with a reduction of collisionality to 0.3 and a correlated increase in trapped particle fraction and bootstrap current density at the edge, the discharges are still closer to the ballooning boundary and their relative distance to the peeling boundary matches approximately the stability result of high collisionality DIII-D discharges. The shear relative to the pressure gradient is so high that an infinite n ballooning analysis with BALOO [39] predicts no access to second stability in agreement with previous studies [12]. Discharges on DIII-D in the low range of collisionality ($\nu_e^* < 0.3$) are typically limited by low n peeling ballooning modes and localized in the nose of the peeling ballooning diagram or on the peeling side [34]. Hence, the lower aspect ratio does not only affect the shape of the peeling ballooning boundary, but for lower collisionality cases shifts the most dominant mode number towards the higher, more ballooning dominated range.

As can be seen in figure 13, showing the radial and poloidal width of the eigenfuctions, the aspect ratio does not significantly affect the spatial extent of the peeling balloning modes. In both cases, the mode is spread on the low field side and most present in the regions of larger curvature.

To conclude, in a direct comparison of pedestal stability between spherical and standard tokamaks at matched shape, current and magnetic field, the lower aspect ratio leads to a stabilization of peeling modes permitting higher j_N.

5. Discussion of results and implications for MAST-U

Over a wide range of pedestal parameters, MAST plasmas have been shown to be ballooning limited in agreement with previous studies. A second relationship between the pedestal height and width, as provided in the EPED model, is needed in combination with the edge stability calculation to predict the pedestal pressure height and width. The investigated discharges lie within a 20% error bar of the predicted pedestal

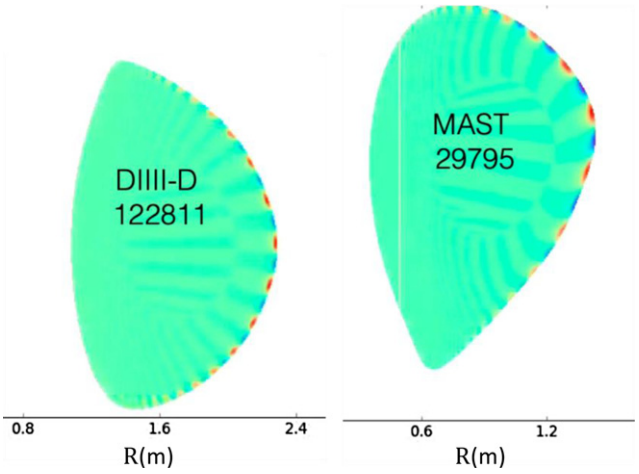

Figure 13. Comparison of radial and poloidal extent of $n = 35$ peeling ballooning mode on DIII-D and MAST.

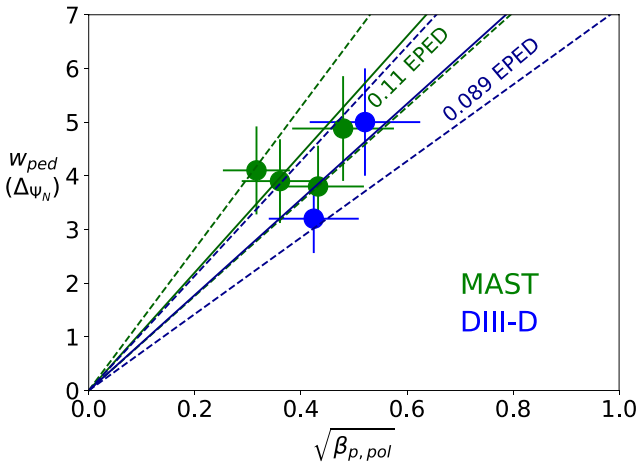

Figure 14. Pedestal width of MAST (green) and DIII-D (blue) vs the square root of pedestal poloidal beta, with the EPED1.6 model predictions shown by dashed lines, for selected equilibria.

width scaling by the EPED1.6 model [46]. The EPED model assumes that pedestals are constrained by onset of nearly local KBMs and global peeling ballooning modes, delivering two equations for the pedestal width and pressure. Using the ballooning critical pedestal technique, EPED calculates a dependence of the pedestal width on the poloidal pedestal beta $\beta_{pol,ped}$ as

$$w_{ped} = G\sqrt{\beta_{pol,\,ped}} \quad (12)$$

with G a function weakly depending on shape, aspect ratio, collisionality and other dimensionless parameters [46]. For the MAST discharges in this dataset a value of $G = 0.11$ (figure 14) is calculated using the ballooning critical pedestal technique. For the DIII-D cases studied here, the G coefficient is slightly smaller at $G = 0.089$.

Assuming that the EPED constraints hold for MAST-U, with a similar value of G (expected operational parameters are listed in table 2 for the initial and late stage), the pedestal pressure can be extrapolated based on a simple beta scaling.

Table 2. Comparison of MAST and MAST-U operational parameter in various stages.

	MAST	MAST-U (initial)	MAST-U (final)
B_T (T)	0.5	0.6	0.75
I_p (MA)	1.3	1.0	2.0
δ	0.45	0.45	0.5
P_{NBI} (MW)	3.8	3.5	5
$t_{discharge}$ (s)	0.6	2	5

Since many MAST DN discharges with similar experimental pedestal pressures around 1.8 kPa were explored in this paper, the high safety factor discharge 29795 among them is selected as starting point for the EPED analysis. A complete analysis with the EPED model predicts a pedestal pressure of 1.73 kPa, in good agreement with the experimental measurement. To scale this discharge to MAST-U, the doubling of the possible plasma current and higher magnetic field strength has to be taken into account.

Previous work on MAST and DIII-D have shown an approximately linear scaling of pedestal height both with plasma current and magnetic field [47, 48], consistent with a constant normalized pedestal beta.

$$\beta_{N,\mathrm{ped}} \sim \frac{p_{\mathrm{ped}}}{B^2 \cdot \frac{I_p a}{B}} \rightarrow p_{\mathrm{ped}} \sim I_p B_T. \tag{13}$$

Using this condition for the approximate functional dependence of peeling ballooning stability $p_{\mathrm{ped}} \sim w_{\mathrm{ped}}^{3/4}$ [47], and the EPED MAST result of 1.73 kPa, the MAST-U pedestal height for matched shaped discharges can be estimated. By combining the peeling ballooning with the kinetic ballooning criterion for the width in equation (12) ($p_{\mathrm{ped}} \sim w_{\mathrm{ped}}^2$), one yields pedestal pressures up to 4.9 kA for the double null discharges (figure 15). In the figure, the dashed lines represent the KBM stability lines, and the peeling ballooning mode threshold is expressed by the solid lines. Note that the green line is with $p_{\mathrm{ped}} \sim w_{\mathrm{ped}}^{3/4}$ is adjusted to intersect with the MAST exp points with a fitting factor, and not based on ELITE calculations. The solid blue and red lines are also $p_{\mathrm{ped}} \sim w_{\mathrm{ped}}^{3/4}$ but just adjusted to meet the $\beta_{N,\mathrm{ped}}$ scaling (equation (13)). For the intermediate level of 1.5 MA current, the predicted pressure amounts to 4.4 kPa on this discharge. The achievable pedestal pressure on MAST-U for this discharge can further benefit from the higher triangularity and increased heating power (table 2). Incorporating these improvements will require a full EPED1.6 simulation in combination with a predictive turbulence and transport model for the plasma core, since the higher heating power will raise core confinement, and hence the Shafranov shift, improving pedestal width. This is left for future work.

This segment has shown that pedestals on MAST as representative of low aspect ratio tokamaks are consistent with EPED model predictions, including the prediction of somewhat wider pedestals at a given $\beta_{\mathrm{pol,ped}}$ than is typical of higher aspect ratio tokamaks such as DIII-D. For a full current and full field discharge repetition on MAST-U, one can assume a tripling of the pedestal pressure as a rule of thumb.

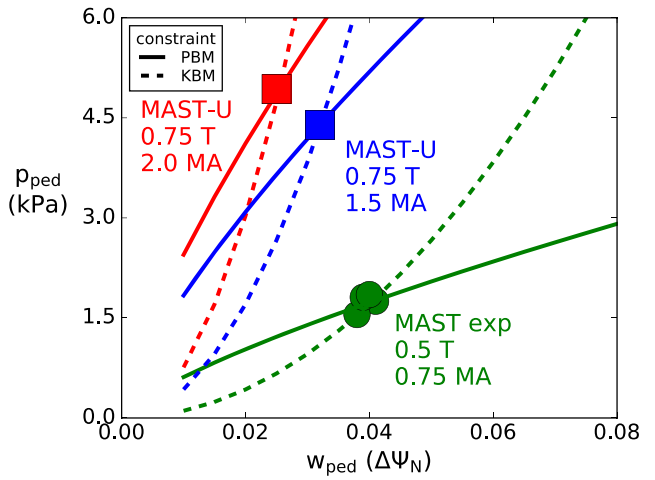

Figure 15. EPED prediction for MAST and MAST-U discharges for various stages of the tokamak. The shape and heating power are assumed to be kept constant.

6. Summary and discussion

Pedestal stability on the low aspect ratio tokamak MAST has been revisited for type I ELM scenarios. Using both experimental ion and electron profiles, kinetic EFITs were reconstructed and investigated for their stability. The following findings were made:

- Over a large pedestal temperature range from 100–300 eV and a collisionality range from 0.3–3.0 MAST equilibria are constrained by high n peeling-ballooning modes with a critical mode number of $n = 25$–45 as shown by the ELITE code.
- Kinetic effects such as FLR stabilization reduce the growth rate of the modes only marginally as calculated by CGYRO confirming the MHD result.
- Plasmas with matched shape on DIII-D show that for similar pedestal conditions the additional shear, Shafranov stabilization, and B/B_p-field ratio on MAST provided by the spherical architecture stabilizes peeling modes and increases ballooning drive.
- The EPED1.6 model predicts that pedestal width in the studied cases on MAST is $w_{\mathrm{ped}} = 0.11\sqrt{\beta_{\mathrm{p,\,pol}}}$, approximately consistent with observations. The width is slightly wider at a given $\beta_{\mathrm{pol,ped}}$ than that typically predicted and observed on higher aspect tokamak such as DIII-D.
- With increased plasma current of up to 2.0 MA and higher magnetic field strength of 0.75 T, pedestal pressures of 4.8 kPa can be reached on MAST-U

Note that peeling mode activity has been experimentally observed and characterized on the spherical tokamak

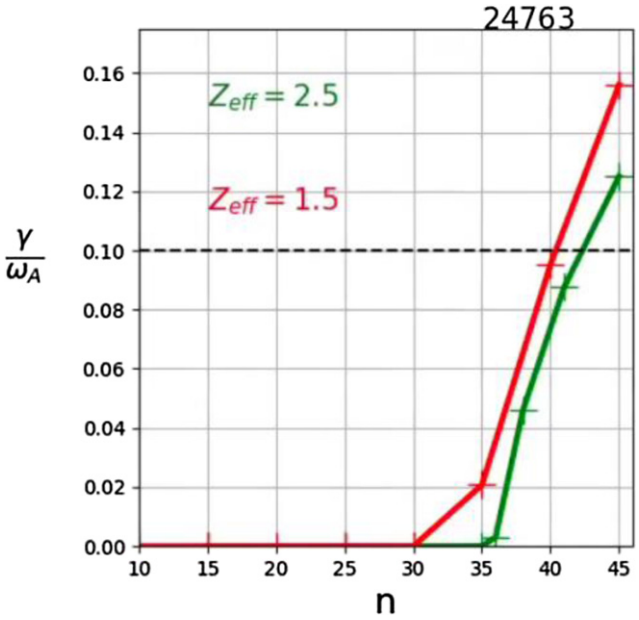

Figure 16. Impact of effective charge on pedestal stability on discharge 24764: growth rates in dependence of mode number for effective charge window from 1.5 (red) to 2.5 (green).

PEGASUS by generating large skin currents during strong plasma current ramps [49]. Hence, an interesting question to be discussed for MAST-U or future power plants based on the ST concept is whether the low aspect ratio machine will be able to reach naturally peeling limited regimes as QH-mode [50] and super H-mode [40, 51]. While the analysis put forward in this paper shows that low aspect ratio machines experience stabilization of the peeling drive, several performance increases of MAST-U are conducive to the access to lower collisionality than presently possible, which would allow a higher bootstrap current and hence operation closer to the peeling boundary:

- Higher toroidal field: in non-dimensional collisionality scans, one typically observes $\nu_e^* \sim B_T^{-4}$, so a field rise by 50% to 0.75 T could deliver a pedestal collisionality reduction by a factor of 5 down below 0.1 for the equilibria analyzed in this paper.
- Higher heating power: 1.2 MW of additional heating power will increase ion and electron temperatures and hence also decrease collisionality.
- Improved shaping: reduced coupling between peeling and ballooning modes associated with strong shaping will allow higher pedestal pressure and eases access to super H-mode [52].

Hence, access to peeling limited regimes as QH-mode and super H-mode could be possible on MAST-U, but will need further and more in depth analysis, which is left for future work. In a similar way, future work will also comprise of further investigating MAST-U discharges with EPED, including shape and heating power. In addition, applying the fitting routines developed here to NSTX and comparing stability results to previous work could provide further insights into low aspect ratio stability. To complete the dataset, DIII-D discharges in MAST shape with lower collisionality will help understand the influence of aspect ratio in the lower collisionality range better.

Disclaimer

Acknowledgments

This material is based upon work supported by the U.S. Department of Energy, Office of Science, Office of Fusion Energy Sciences, using the DIII-D National Fusion Facility, a DOE Office of Science user facility, under Awards DE-FC02-04ER54698, DE-SC0018030, DE-SC0018287, DE-SC0018990. Part of the data analysis was performed using the OMFIT integrated modeling framework [53]. We gratefully acknowledge the support of the DIII-D Team for tokamak, auxiliary heating, and diagnostic systems operation. This project has also received funding from the Engineering and Physical Sciences Research Council (EPSRC) of the UKRI program (Grant No. EP/T012250/1).

Data availability statement

Raw data were generated at the DIII-D national fusion facility. Derived data supporting the findings of this study are available from the corresponding author upon reasonable request.

Appendix A. Influence of effective charge

To investigate the validity of the stability analysis conducted in this paper with regards to the choice of effective charge, the influence of Z_{eff} will be analyzed. For this purpose, a low safety factor equilibrium is chosen and analyzed assuming an effective charge of (a) $Z_{\mathrm{eff}} = 1.5$ and (b) $Z_{\mathrm{eff}} = 2.5$ (figure 16). While the general result of the pedestal being limited by medium to high n ballooning modes is conserved, the most unstable mode number is affected and increasing with effective charge, respectively decreasing with lower pedestal pressure. Hence, in order to proof that MAST pedestals are ballooning limited, the effective charge has to be chosen in a way that within the possible frame of choice of Z_{eff} the outcome is least ballooning limited, hence $Z_{\mathrm{eff}} = 1.5$ has to be assumed. This will ensure that the actual experimental equilibrium with

equal or higher effective charge is similarly or even stronger limited by ballooning modes. Note that the quantitative effect is not significant and the change in mode number within the experimental uncertainty level of 20%.

ORCID iDs

M. Knolker https://orcid.org/0000-0002-8468-8767
S. Henderson https://orcid.org/0000-0002-8886-1256
A. Kirk https://orcid.org/0000-0002-5746-6595
S. Saarelma https://orcid.org/0000-0002-6838-2194
P.B. Snyder https://orcid.org/0000-0002-0613-4232

References

[1] Peng Y.-K.M. 2000 The physics of spherical torus plasmas *Phys. Plasmas* **7** 1681–92
[2] Peng Y.-K.M. and Strickler D.J. 1986 Features of spherical torus plasmas *Nucl. Fusion* **26** 769–77
[3] Menard J.E., Jardin S.C., Kaye S.M., Kessel C.E. and Manickam J. 1997 Ideal MHD stability limits of low aspect ratio tokamak plasmas *Nucl. Fusion* **37** 595–610
[4] Costley A.E. 2019 Towards a compact spherical tokamak fusion pilot plant *Phil. Trans. R. Soc.* A **377** 20170439
[5] Wagner F. *et al* 1982 Regime of improved confinement and high beta in neutral-beam-heated divertor discharges of the ASDEX tokamak *Phys. Rev. Lett.* **49** 1408–12
[6] Kinsey J.E., Staebler G.M., Candy J., Waltz R.E. and Budny R.V. 2011 ITER predictions using the GYRO verified and experimentally validated trapped gyro-Landau fluid transport model *Nucl. Fusion* **51** 083001
[7] Zohm H. 1996 Edge localized modes (ELMs) *Plasma Phys. Control. Fusion* **38** 105–28
[8] Leonard A.W. 2014 Edge-localized-modes in tokamaks *Phys. Plasmas* **21** 090501
[9] Snyder P.B. *et al* 2002 Edge localized modes and the pedestal: a model based on coupled peeling-ballooning modes *Phys. Plasmas* **9** 2037–43
[10] Sykes A. *et al* 2001 First results from MAST *Nucl. Fusion* **41** 1423–33
[11] Saarelma S., Hender T.C., Kirk A., Meyer H., Wilson H.R. and Team M. 2007 MHD stability analysis of ELMs in MAST *Plasma Phys. Control. Fusion* **49** 31–42
[12] Dickinson D., Saarelma S., Scannell R., Kirk A., Roach C.M. and Wilson H.R. 2011 Towards the construction of a model to describe the inter-ELM evolution of the pedestal on MAST *Plasma Phys. Control. Fusion* **53** 115010
[13] Kirk A., O'Gorman T., Saarelma S., Scannell R. and Wilson H.R. 2009 A comparison of H-mode pedestal characteristics in MAST as a function of magnetic configuration and ELM type *Plasma Phys. Control. Fusion* **51** 065016
[14] Ono M. *et al* 2001 Overview of the initial NSTX experimental results *Nucl. Fusion* **41** 1435–47
[15] Diallo A. *et al* 2013 Progress in characterization of the pedestal stability and turbulence during the edge-localized-mode cycle on national spherical torus experiment *Nucl. Fusion* **53** 093026
[16] Sontag A.C. *et al* 2011 Pedestal characterization and stability of small-ELM regimes in NSTX *Nucl. Fusion* **51** 103022
[17] Maingi R. *et al* 2009 Edge-localized-mode suppression through density-profile modification with lithium-wall coatings in the national spherical torus experiment *Phys. Rev. Lett.* **103** 075001
[18] Harrison J.R. *et al* 2019 Overview of new MAST physics in anticipation of first results from MAST Upgrade *Nucl. Fusion* **59** 112011
[19] Luxon J.L. 2002 A design retrospective of the DIII-D tokamak *Nucl. Fusion* **42** 313
[20] Walsh M.J., Arends E.R., Carolan P.G., Dunstan M.R., Forrest M.J., Nielsen S.K. and O'Gorman R. 2003 Combined visible and infrared Thomson scattering on the MAST experiment *Rev. Sci. Instrum.* **74** 1663–6
[21] Scannell R., Walsh M.J., Carolan P.G., Conway N.J., Darke A.C., Dunstan M.R., Hare D. and Prunty S.L. 2006 Enhanced edge Thomson scattering on MAST *Rev. Sci. Instrum.* **77** 10E510
[22] Stammers K. and Loughlin M.J. 2006 The calibration of the MAST neutron yield monitors *Nucl. Instrum. Methods Phys. Res. Sect. A Accel. Spectrom. Detect. Assoc. Equip.* **562** 521–30
[23] Groebner R.J. and Osborne T.H. 1998 Scaling studies of the high mode pedestal *Phys. Plasmas* **5** 1800–6
[24] McCone J., Conway N.J., Von Hellermann M., Field A.R., Garzotti L., Michael C.A., Patel A., Scannell R. and Wisse M. 2010 Carbon Transport in MAST *37th EPS Conf. on Plasma Physics 2010* (Dublin, Ireland, June 22–25) (http://ocs.ciemat.es/EPS2014PAP/pdf/P5.054.pdf)
[25] Henderson S.S. *et al* 2015 Charge dependence of neoclassical and turbulent transport of light impurities on MAST *Plasma Phys. Control. Fusion* **57** 095001
[26] Hawryluk R.J. 1981 AN empirical approach to tokamak transport *Physics of Plasmas Close to Thermonuclear Conditions* (Amsterdam: Elsevier) pp 19–46
[27] Breslau J., Gorelenkova M., Poli F., Sachdev J. and Yuan X. 2018 TRANSP Computer Software, USDOE Office of Science (SC), Fusion Energy Sciences (FES) (SC-24) https://doi.org/10.11578/dc.20180627.4
[28] Conway N.J., Carolan P.G., McCone J., Walsh M.J. and Wisse M. 2006 High-throughput charge exchange recombination spectroscopy system on MAST *Rev. Sci. Instrum.* **77** 10F131
[29] Lao L.L., St. John H., Stambaugh R.D., Kellman A.G. and Pfeiffer W. 1985 Reconstruction of current profile parameters and plasma shapes in tokamaks *Nucl. Fusion* **25** 1611–22
[30] Sauter O., Angioni C. and Lin-Liu Y.R. 1999 Neoclassical conductivity and bootstrap current formulas for general axisymmetric equilibria and arbitrary collisionality regime *Phys. Plasmas* **6** 2834–9
[31] Miller R.L., Chu M.S., Greene J.M., Lin-Liu Y.R. and Waltz R.E. 1998 Noncircular, finite aspect ratio, local equilibrium model *Phys. Plasmas* **5** 973–8
[32] Connor J.W., Hastie R.J. and Taylor J.B. 1978 Shear, periodicity, and plasma ballooning modes *Phys. Rev. Lett.* **40** 396–9
[33] Osborne T.H. *et al* 2015 Enhanced H-mode pedestals with lithium injection in DIII-D *Nucl. Fusion* **55** 063018
[34] Knolker M. *et al* 2018 Investigation of the role of pedestal pressure and collisionality on type-I ELM divertor heat loads in DIII-D *Nucl. Fusion* **58** 096023
[35] Candy J., Belli E.A. and Bravenec R.V. 2016 A high-accuracy Eulerian gyrokinetic solver for collisional plasmas *J. Comput. Phys.* **324** 73–93
[36] Belli E.A. and Candy J. 2018 Impact of centrifugal drifts on ion turbulent transport *Phys. Plasmas* **25** 032301
[37] Dickinson D., Roach C.M., Saarelma S., Scannell R., Kirk A. and Wilson H.R. 2012 Kinetic instabilities that limit β in the edge of a tokamak plasma: a picture of an H-mode pedestal *Phys. Rev. Lett.* **108** 135002
[38] Beurskens M.N.A. *et al* 2011 H-mode pedestal scaling in DIII-D, ASDEX Upgrade, and JET *Phys. Plasmas* **18** 056120
[39] Miller R.L., Lin-Liu Y.R., Turnbull A.D., Chan V.S., Pearlstein L.D., Sauter O. and Villard L. 1997 Stable equilibria for bootstrap-current-driven low aspect ratio tokamaks *Phys. Plasmas* **4** 1062–8

[40] Snyder P.B. *et al* 2019 High fusion performance in super H-mode experiments on Alcator C-Mod and DIII-D *Nucl. Fusion* **59** 086017
[41] Lortz D. 1975 The general 'peeling' instability *Nucl. Fusion* **15** 49–54
[42] Wesson J.A. 1978 Hydromagnetic stability of tokamaks *Nucl. Fusion* **18** 87–132
[43] Connor J.W., Hastie R.J., Wilson H.R. and Miller R.L. 1998 Magnetohydrodynamic stability of tokamak edge plasmas *Phys. Plasmas* **5** 2687–700
[44] Cooper A. 1992 Variational formulation of the linear MHD stability of 3D plasmas with noninteracting hot electrons *Plasma Phys. Control. Fusion* **34** 1011–36
[45] Chapman I.T., Simpson J., Saarelma S., Kirk A., O'Gorman T. and Scannell R. 2015 The stabilizing effect of core pressure on the edge pedestal in MAST plasmas *Nucl. Fusion* **55** 013004
[46] Snyder P.B., Groebner R.J., Hughes J.W., Osborne T.H., Beurskens M., Leonard A.W., Wilson H.R. and Xu X.Q. 2011 A first-principles predictive model of the pedestal height and width: development, testing and ITER optimization with the EPED model *Nucl. Fusion* **51** 103016
[47] Snyder P.B., Wilson H.R., Osborne T.H. and Leonard A.W. 2004 Characterization of peeling-ballooning stability limits on the pedestal *Plasma Phys. Control. Fusion* **46** A131–41
[48] Diallo A., Scannell R., Saarelma S., Kirk A., Hillesheim J.C., Crocker N. and Dunai D. (The MAST Team) 2014 Pedestal evolution and scaling with plasma current on MAST *41st EPS Conf. on Plasma Physics* (Berlin, Germany, June 23–27) p P5.054 (http://ocs.ciemat.es/EPS2014PAP/pdf/P5.054.pdf)
[49] Bongard M.W., Thome K.E., Barr J.L., Burke M.G., Fonck R.J., Hinson E.T., Redd A.J. and Schlossberg D.J. 2014 Characterization of peeling modes in a low aspect ratio tokamak *Nucl. Fusion* **54** 114008
[50] Burrell K.H. *et al* 2002 Quiescent H-mode plasmas in the DIII-D tokamak *Plasma Phys. Control. Fusion* **44** 325
[51] Knolker M. *et al* 2021 On the stability and stationarity of the super H-mode combined with an ion transport barrier in the core *Plasma Phys. Control. Fusion* **63** 025017
[52] Knolker M. *et al* 2020 Optimizing the super H-mode pedestal to improve performance and facilitate divertor integration *Phys. Plasmas* **27** 102506
[53] Logan N.C., Grierson B.A., Haskey S.R., Smith S.P., Meneghini O. and Eldon D. 2018 OMFIT tokamak profile data fitting and physics analysis *Fusion Sci. Technol.* **74** 125–34